

A New 3-D Automated Computational Method to Evaluate In-Stent Neointimal Hyperplasia in In-Vivo Intravascular Optical Coherence Tomography Pullbacks

Serhan Gurmeric¹, Gozde Gul Isguder¹, Stéphane Carlier², and Gozde Unal¹

¹ Faculty of Engineering and Natural Sciences, Sabanci University, Istanbul, Turkey
gozdeunal@sabanciuniv.edu

² St Maria hospital, Halle and UZ Brussel, Belgium

Abstract. Detection of stent struts imaged in vivo by optical coherence tomography (OCT) after percutaneous coronary interventions (PCI) and quantification of in-stent neointimal hyperplasia (NIH) are important. In this paper, we present a new computational method to facilitate the physician in this endeavor to assess and compare new (drug-eluting) stents. We developed a new algorithm for stent strut detection and utilized splines to reconstruct the lumen and stent boundaries which provide automatic measurements of NIH thickness, lumen and stent area. Our original approach is based on the detection of stent struts unique characteristics: bright reflection and shadow behind. Furthermore, we present for the first time to our knowledge a rotation correction method applied across OCT cross-section images for 3D reconstruction and visualization of reconstructed lumen and stent boundaries for further analysis in the longitudinal dimension of the coronary artery. Our experiments over OCT cross-sections taken from 7 patients presenting varying degrees of NIH after PCI illustrate a good agreement between the computer method and expert evaluations: Bland-Altman analysis revealed a mean difference for lumen cross-section area of $0.11 \pm 0.70mm^2$ and for the stent cross-section area of $0.10 \pm 1.28mm^2$.

1 Introduction

Optical Coherence Tomography (OCT) is a recent modality, which measures the intensity of back-reflected infrared light instead of acoustical waves using an interferometer since the speed of light is much faster than that of sound [1]. OCT was found useful as an intravascular imaging technique, and compared to IVUS in several works [2,3]. The biggest advantage of OCT is its high resolution, on the order of 15 microns spatially, but at the cost of a decreased penetration depth of 1mm to 2mm. Both in vitro and in vivo studies [2,4] have shown that the resolution of OCT can differentiate between typical constituents of atherosclerotic plaques, such as lipid, calcium, and fibrous tissue better than IVUS [5], and can also resolve the thin fibrous cap that is thought to be responsible for plaque vulnerability[6].

Although Drug Eluting Stents (DES) suppress NeoIntimal Hyperplasia (NIH) strongly, in-stent restenosis after DES implantation still occurs [7]. Studies have shown that nonuniform circumferential stent strut distribution affects local drug concentration [8]. Number and distribution of the stent struts might also affect the magnitude of NIH after stent implantation in human coronary arteries [9]. Therefore, tracking of stent position/malapposition and neointimal tissue growth after stent implantation is clinically important.

To our knowledge, besides studies of stents by IVUS, there are no studies of strut distribution analysis on intracoronary OCT pullbacks to assist in the assessment of the degree of restenosis. The objective of this study was three-fold: (i) to explore the usability and performance of automatic computer methods to help with stent strut analysis in varying degrees of NIH scenarios; (ii) to compare the computer analysis with expert analysis to correlate the results in OCT images; (iii) to carry the 2D OCT pullback analysis to longitudinal dimension in 3D.

2 Method

OCT Imaging Protocol. Automated pullbacks at 1 mm/s were conventionally performed using a M2 OCT Imaging System (LightLab Imaging, Inc., Westford, MA, USA) running at a frame rate of 15.6/sec and a dedicated fibre-optic imaging wire (ImageWireTM, LightLab Imaging Inc., Westford, MA, USA). Temporary blood clearance was obtained with a proximal occlusion balloon inflated to between 0.5-0.7 atm, while simultaneously flushing physiological saline through the distal lumen of the balloon catheter at a rate of 0.5ml/s. Images have an axial resolution of about 15 microns. In vivo OCT pullbacks were recorded as rectangular images of 200x752 pixels (200 angles with 752 samples each on each ray). These rectangular images were processed by our method and displayed after scan-conversion in a standard viewing format.

Study Population. Seven pullbacks performed in previously stented coronary segments of seven patients presenting varying degrees of NIH were the test cases of our automated methods.

2.1 OCT Pullback Image Analysis

Our approach consists of four different main parts: (i) preprocessing OCT cross-section images; (ii) initializing and propagating a spline inside the lumen region; (iii) detection of struts and reconstruction of the stent boundary; (iv) registration between consecutive OCT images for 3D reconstruction, and measurements for assessment of in-stent restenosis.

Preprocessing. It can be observed in a typical OCT image that brighter pixel groups represent vessel wall, plaque, and stent struts (Fig. 1). To enhance the desired information in the image, a 50 percentile of the histogram is selected as a threshold, and the image is thresholded followed by a median and a Gaussian filter to enhance and smooth the regions with struts and their shadows around the lumen (Fig 1-b and c).

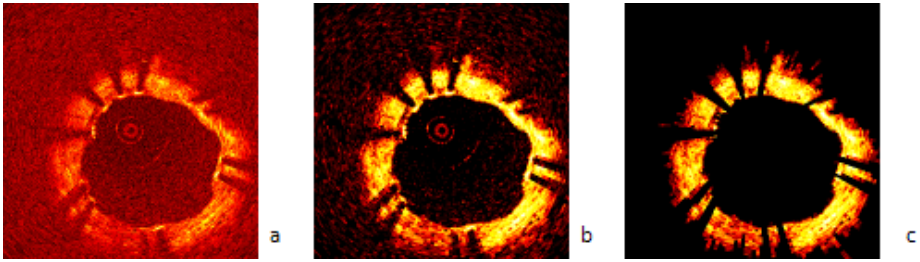


Fig. 1. (a) OCT display image; (b) Thresholded image; (c) Denoised image

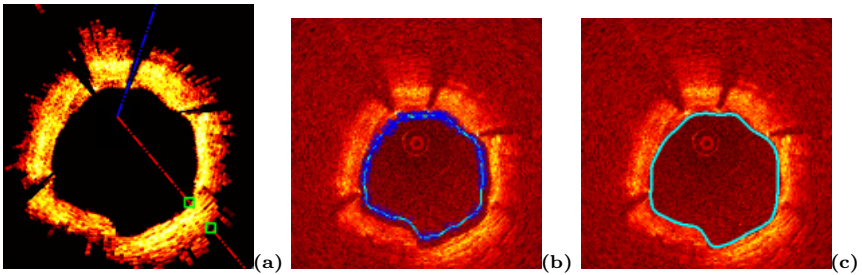


Fig. 2. (a) Ray shooting in prefiltered image; (b) Initial spline on ray intersection points; (c) Spline evolution and segmented lumen region

Lumen Segmentation. We developed a new and problem specific method for segmentation of the lumen region on an OCT cross-section image and creation of a band or a region of interest (ROI) in the arterial wall behind the lumen boundary, which facilitates stent strut detection. Particularly, strut shadows in this ROI are essential clues utilized in our algorithm. To segment the lumen region, we utilized a Catmull-Rom spline, which has four polynomial blending functions and whose control points are exactly on the spline contour. The interaction and initialization of this cubic hermite spline are practically well-suited to our problem for correction of the lumen contour and stent splines, if necessary.

Spline Initialization and Propagation. For detection of the ROI, i.e. the inner and outer boundaries of the observable bright band in the OCT image, we utilize two splines, and initialize the spline control points by shooting rays on the rectangular domain “denoised image” from the center coordinates of the display image to every angle, and analyzing the thickness of the ROI region in the arterial wall (Fig. 2-a). Two Catmull-Rom splines are constructed to separate strut and shadow zone of image. The control points are initialized at the inner side of the ROI (Fig. 2-b), and the spline propagates towards the lumen border and stops on the desired boundaries via an edge-based active contour framework as exemplified in Fig. 2-c.

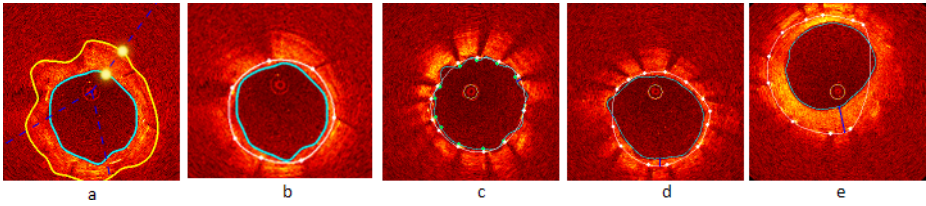


Fig. 3. (a) The ROI with start and end points for energy calculations; (b) Detected struts; Examples of strut detection, lumen and stent boundary reconstruction in 3 different scenarios: (c) NIH absent; (d) minimum amount of NIH; (e) moderate amount of NIH

Shadow and Strut Detection. One important observation is that the OCT cross-section images which contain stent struts, generally include shadows behind the struts. Analyzing the angular intensity energy distribution in the ROI provides clues to these shadows. To build such an energy map, rays from the image center are extended and the intersection points of these rays and the splines are computed. Interpolation of these two intersection coordinates (Fig. 3-a) and summation of corresponding image intensity values define the energy on a ray. Energy distribution over all the rays are analyzed: falling and rising of energy on these rays indicates the presence and absence of strut shadows. A second analysis over the detected shadow rays is carried out between the two splines to detect the exact strut positions over the original image. A strut on a shadow ray is the maximum bright intensity pixel group and mostly negative deep gradient vectors follow such a group (Fig. 3-b). The stent boundary is reconstructed by fitting another Catmull-Rom spline to the detected struts.

For different NIH scenarios, we designed two modes of our system: (i) the new stent implants and minimum NIH cases; (ii) mild to severe NIH cases. The shadow and strut detection then differs w.r.t. the interpolation of the angular energy calculation: either starts from first spline to the middle range of the ROI, or from the middle of the ROI towards the outer field, respectively. Thus the search range varies and the strut detection threshold parameters are heuristically determined and fixed for both modes (mode 1: 30% energy fall, 45% energy rise; mode 2: 45% energy fall, 35% energy rise) for all the experiments. A simple mode picking operation changes these parameters in the application. Examples are shown in Fig. 3 for strut detection, lumen and stent boundary reconstruction in three different scenarios: (c) virtually no NIH; (d) minimum amount of NIH; (e) moderate amount of NIH.

Calibration. Calibration of the OCT images was based on the known physical dimension of the imaging sheath (0.0019") inside which the fibre-optic rotates and that is visualized as a small circle in the middle of the display image and as a line on the rectangular image.

2.2 3D Reconstruction in the Longitudinal Dimension

During a pullback, as the catheter moves inside the arteries in-vivo, it inevitably translates and rotates and causes a misalignment between the two recorded

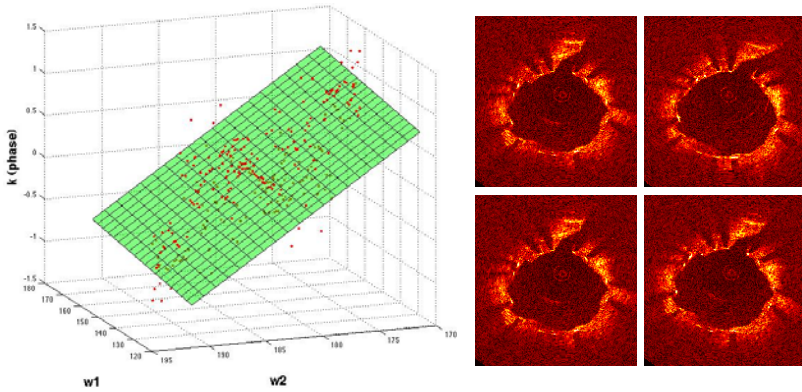


Fig. 4. Rotation estimation: Middle column: source image; Right top: reference image; Right bottom: rotated source image with the estimated rotation=-5.21 degrees; Left: fitted plane to phase ρ

consecutive cross-section images. Moreover, the catheter may go back and forth as the heart dilates and compresses. The result is a pulsatile and jagged longitudinal geometry of the vessel wall (see Fig 6-a). For an accurate 3D vessel geometry and longitudinal analysis, these catheter effects should be corrected. We address two of the cross-sectional catheter motion. The first is the translation of the catheter in the lumen due to varying vessel curvature. We account for this by aligning the OCT cross-section images w.r.t. their lumen border center of mass.

To address the rotation of the catheter during pullback, we estimated rotation between subsequent frames via a spectral correlation analysis method inspired by [10], where the translation on a rectangular image, which corresponds to a rotation on the display image, is calculated as follows: Let I be the rectangular image and I_t is the translated version of I with a 2D translation $\mathbf{t} = (t_1, t_2)$. The ratio between the Fourier transforms of the image I and I_t : $k(w_1, w_2) = F(I_t)/F(I).e^{-j\langle \mathbf{w}, \mathbf{t} \rangle}$, can be used to extract the phase: $\rho(\mathbf{w}) = \langle \mathbf{w}, \mathbf{t} \rangle = w_1 * t_1 + w_2 * t_2$, where $\mathbf{w} = (w_1, w_2)$ denotes the 2D frequency vector. The idea then is to estimate the amount of shift using the phase defined over the 2D frequency space by fitting a plane to the ρ function: $Aw_1 + Bw_2 + C\rho = D$. Here a translation between the two images in either the horizontal or the vertical direction can be detected over the plane aligned with one of the frequency axis w_1 or w_2 . Practically, a least-squares estimator is used via a singular value decomposition. In the OCT rectangular images, the calculated slope B of the plane represents the estimated rotation value in radians (whereas $D=0$). In Fig. 4 an example is shown for rotation estimation between two subsequent OCT frames.

After the 2D registration, we reconstruct the 3D geometry of the stent and lumen borders by building triangular meshes over the stack of 2D rotated splines. On top of these, we render the stent struts approximated by a thin ellipsoid geometry. Our future goal here is to obtain 3D models of stent meshes, however,

for the current work, we accounted for the lack of a mesh model by a filtering to eliminate struts that violate certain distance conditions away from the neighbor strut on adjacent frames. A transparent stent tube model is deformed to fit detected struts as will be depicted in the Results.

3 Results and Discussions

3.1 Assessment of Strut Distribution

39 OCT cross-sections from 7 pullbacks of 7 patients presenting varying degrees of NIH are selected. Manual strut detection is carried out by the expert in two ways: (i) via manual tracing using the reviewing software provided by the OCT manufacturer (LightLab Imaging, MA, USA), called as LL software here and taken as the gold standard; (ii) using our system with correction over the automatic results (the extracted splines can be corrected, stent struts can be added, removed or marked), abbreviated as the SF (Stent Follow-up) system. The two manual analysis (LL and SF) are compared with the automatic detection (ASF: Automatic Stent Follow-up) over this image set.

Figure 5 depicts a diagram for the measurements carried out in our experiments for the strut assessment. First, we count the total number of detected struts in each cross-section image. The percentage of correctly detected struts is set to $1 - \text{normalized error}$, where the normalized error = $|\#\text{struts marked by the physician} - \#\text{struts detected by our algorithm}| / |\#\text{struts marked by the physician}|$. Another parameter measured is the maximum angle between adjacent stent struts. As reported by Takebayashi et al. [9], this measurement correlates with the NIH thickness in IVUS-based studies. NIH thickness was also evaluated looking at the lumen cross-sectional area (L-CSA), the stent cross-sectional area (S-CSA), minimum, maximum, and average distance between the lumen boundary and the stent. Finally, stent eccentricity was calculated as the minimum divided by the maximum stent diameter.

Table 1 presents measurements of the lumen and the stent CSAs, and the number of stent struts with a comparison between the automatic detection (ASF), the expert's adjustment of the automatic results (SF), and the expert's manual measurements using the LightLab software (LL). Table 2 presents the rest of the measurements: the maximum inter-strut angle, the minimum, average, and maximum distances between the stent and the lumen borders, and the stent eccentricity, which were not available from the LL software.

Very good agreements were found between the computer methods and the expert evaluations for lumen CSA (mean difference following Bland-Altman = $0.11 \pm 0.70\text{mm}^2$; $r^2 = 0.98$, $p < 0.0001$) and the stent CSA (mean difference = $0.10 \pm 1.28\text{mm}^2$; $r^2 = 0.85$, $p < 0.0001$). The average number of detected struts was 10.4 ± 2.9 per cross-section when the expert identified 10.5 ± 2.8 ($r^2 = 0.78$, $p < 0.0001$), with an overall accuracy in strut detection of $91 \pm 11\%$. For the given patient dataset: lumen CSA was on the average $6.05 \pm 1.87\text{mm}^2$, stent CSA was $6.26 \pm 1.63\text{mm}^2$, maximum angle between struts was on the average $85.96 \pm 54.23^\circ$, maximum, average, and minimum distance between the stent and

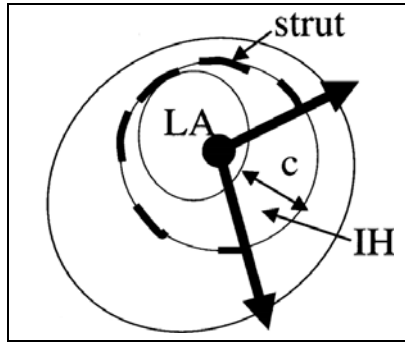


Fig. 5. Schematic of struts and related measurements calculated for stent follow-up analysis, adapted from [9]. Maximum interstrut angle, LA (lumen cross-sectional area: L-CSA), IH (=Stent CSA - L-CSA), distances between the lumen and the stent contours (here *c* is depicted: the maximum distance=thickness of the NIH).

Table 1. Strut assessment measurements compared among the expert manual detection with two different systems and the automatic detection. Values are mean ± std. ASF: Autodetection, SF: Expert manual adjustment, LL: Expert manual measurement.

	ASF	SF	LL
Lumen CSA, mm^2	5.78±1.76	6.09±1.85	6.05±1.87
Stent CSA, mm^2	6.59±1.91	6.33±1.66	6.26±1.63
Stent struts, <i>n</i> normalized to (0,1)	0.91±0.11	1.00±0.00	1.00±0.00

Table 2. Other strut assessment measurements compared between the expert manual detection and the automatic detection with our system. Values are mean ± std.

	ASF	SF
Max angle btw stent struts, °	75.09±26.63	85.96±54.23
Max distance btw stent and lumen border, mm	0.31±0.15	0.18±0.13
Avg distance btw stent and lumen border, mm	0.14±0.07	0.08±0.06
Min distance btw stent and lumen border, mm	0.02±0.04	0.01±0.02
Stent eccentricity	0.75±0.11	0.80±0.08

the lumen were $0.18 \pm 0.13mm$, $0.08 \pm 0.06mm$, and $0.01 \pm 0.02mm$, respectively, and stent eccentricity was 0.80 ± 0.08 .

Due to possible hindering of shadows by severe NIH, strut detection and stent boundary reconstruction becomes more challenging and more prone to errors than that of the lumen. This difficulty caused a lower match between the automatic and manual computations based on the stent boundary such as

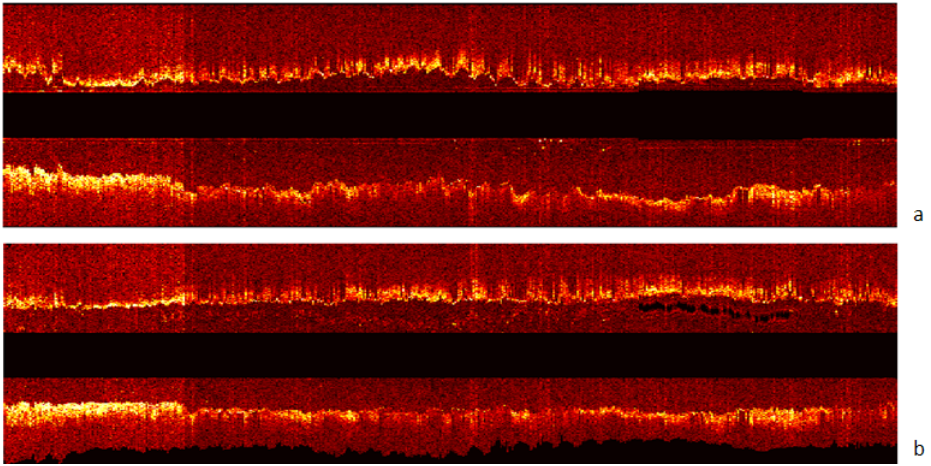


Fig. 6. Longitudinal cut view: (a) original; (b) center and rotation aligned pullback

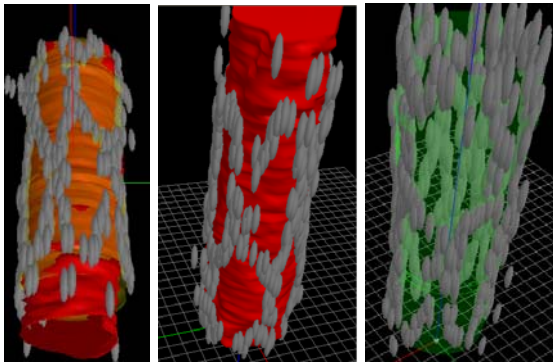


Fig. 7. Examples of 3D Reconstruction of the lumen boundary (red surface), the stent boundary (yellow surface depicted on the left) and the stent struts represented as gray ellipsoids. Green transparent mesh on the right represents the vessel wall.

the maximum distance calculation between the stent and the lumen border as observed in Table 2. Our work is ongoing for further improvements on such struts, which were missed with the shadow detection.

3.2 3D Reconstruction

The performance of the 2D OCT registration method (Sec 2.2) is validated on synthetic images: a binary ellipse image is generated and rotated with a known value to generate a second ellipse image, then the spectral correlation method is used to estimate the amount of rotation. The results were $\approx 98.5\%$ accurate for up to rotations of 0.8 radians. The proposed method has been applied to OCT pullbacks

to account for catheter cross-sectional motion. Fig. 6 depicts a longitudinal view from the original pullback (a), the center and rotation aligned pullback (b), where the reduced jaggedness in the lumen boundaries can be observed.

Next, a 3D visualization is shown in Fig. 7 for the reconstructed lumen surface, and stent struts as a surface rendering. The mesh pattern of the stent is visible and presents a possibility of examining the 3D position of the stent w.r.t. the lumen boundary. We are currently working on including a 3D mesh model of the original stent for 3D stent analysis.

4 Conclusions

We presented a new spline-based segmentation for both the lumen and the stent boundaries, and an energy map based automatic stent strut detection algorithm in OCT pullbacks, to assist in the problem of strut distribution assessment. Our experimental results demonstrated that our algorithm works reasonably well on the segmentation of target boundaries in OCT images, and detected stent struts and their trailing shadows. A strut distribution analysis was carried out and a number of measures important for stent implant follow-up and monitoring of the neointimal tissue growth over struts were calculated. An extension to a 3D/longitudinal analysis is also illustrated. Part of our ongoing and future studies include extension of the spline segmentation to 3D, and using previously constructed models of stent meshes.

The conclusion from our study is that our new methods appear to offer a robust and reliable automated analysis of OCT pullbacks of coronary stented segments that might assist physicians in evaluating in-stent restenosis after PCI and study the vascular response of new stents and eluted drugs. A large-scale evaluation of OCT pullback stent analysis will be necessary to further correlate the degree of NIH and circumferential stent strut distribution, as suggested previously by IVUS [9].

References

1. Barlis, P., Schmitt, J.: Current and future developments in intracoronary optical coherence tomography imaging. *EuroIntervention* 4, 529–534 (2008)
2. Jang, I.: et al: Visualization of coronary atherosclerotic plaques in patients using optical coherence tomography: Comparison with intravascular ultrasound. *American Journal of Cardiology* 39, 604–609 (2002)
3. Patwari, P.: et al: Assessment of coronary plaque with optical coherence tomography and high-frequency ultrasound. *American Journal of Cardiology* 85, 641–644 (2000)
4. Yabushita, H.: et al: Characterization of human atherosclerosis by optical coherence tomography. *Circulation* 106, 1640–1645 (2002)
5. Rieber, J., Meissner, O., Babaryka, G., Oswald, S.R.M., Koenig, A., Schiele, T., Shapiro, M., Theisen, K., Reiser, M., Klauss, V., Hoffmann, U.: Diagnostic accuracy of optical coherence tomography and intravascular ultrasound for the detection and characterization of atherosclerotic plaque composition in ex-vivo coronary specimens: a comparison with histology. *Coronary Artery Disease* 17(5), 425–430 (2006)

6. Xu, C., Schmitt, J., Carlier, S., Virmani, R.: Characterization of atherosclerosis plaques by measuring both backscattering and attenuation coefficients in optical coherence tomography. *Journal of Biomedical Optics* 13(3) (2008)
7. Lemos, P., Saia, F., Ligthart, J., Arampatzis, C., Sianos, G., Tanabe, K., Hoye, A., Degertekin, M., Daemen, J., McFadden, E., Hofma, S., Smits, P., de Feyter, P., van der Giessen, W., van Domburg, R., Serruys, P.: Coronary restenosis after sirolimus-eluting stent implantation: morphological description and mechanistic analysis from a consecutive series of cases. *Circulation* 108, 257–260 (2003)
8. Hwang, C.W., Wu, D., Edelman, E.R.: Physiological transport forces govern drug distribution for stent-based delivery. *Circulation* 104, 600–605 (2001)
9. Takebayashi, H., Mintz, G., Carlier, S., Kobayashi, Y., Fujii, K., Yasuda, T., Costa, R., Moussa, I., Dangas, G., Mehran, R., Lansky, A., Kreps, E., Collins, M., Colombo, A., Stone, G., Leon, M., Moses, J.: Nonuniform strut distribution correlates with more neointimal hyperplasia after sirolimus-eluting stent implantation. *Circulation* 110, 3430–3434 (2004)
10. Hernandez, A., Radeva, P., Tovar, A., Gil, D.: Vessel structures alignment by spectral analysis of IVUS sequences. In: *Proceedings of Computer Vision for Intravascular and Intracardiac Imaging, CVII* (2006)